Redshift and optical anisotropy of collective π-volume modes in multiwalled carbon nanotubes

A. Seepujak,[1,*] U. Bangert,[1] A. J. Harvey,[1] P. M. F. J. Costa,[2] and M. L. H. Green[2]
[1]*Department of Physics, University of Manchester, Oxford Road, Manchester M13 9PL, United Kingdom*
[2]*Inorganic Chemistry Laboratory, University of Oxford, South Parks Road, Oxford OX1 3QR, United Kingdom*
(Received 21 September 2005; revised manuscript received 22 May 2006; published 1 August 2006)

A combined study concerning localized electron energy-loss spectroscopy (EELS) and modeling of collective π-volume modes in multiwalled carbon nanotubes (MWCNT) is presented. The changing line width and eigenfrequency of the π-volume mode can be ascribed solely to optical anisotropy and "cylindrical anisotropy." Optical anisotropy results from the weighting of various nearly degenerate and nondegenerate states allowed for the $\mathbf{E}_{\|c}$ and $\mathbf{E}_{\perp c}$ polarizations. Cylindrical anisotropy arises from a lowering of the symmetry arising from the nanotube geometry. The eigenfrequency of the π-volume mode corresponds to polarization eigenmodes of graphite, and not to new maxima in the joint density of states, since momentum transfer $\Delta\mathbf{q}_{\pi}\rightarrow 0$. Results are also included from multiwalled hexagonal-boron nitride nanotubes (MWBNNT). An accurate description of the π-volume mode in multiwalled nanotubes has not been attempted so far, and is essential to resolve coupled MWCNT π-surface features, which are usually obscured in spectra obtained in penetrating-beam geometry. Volume mode-extracted EEL spectra demonstrate eigenfrequency modification of coupled π-surface features in the presence of a MWCNT dielectric filling. It was found, owing to dielectric screening effects and smearing of the dipole mode, that aloof-beam EELS which is conventionally applied to surface plasmon investigations, cannot give this information.

DOI: 10.1103/PhysRevB.74.075402 PACS number(s): 73.21.−b, 73.22.Lp, 68.37.Lp

I. INTRODUCTION

Tuning the eigenenergy of collective resonances in multiwalled carbon nanotubes (MWCNTs) is an issue of immense interest: MWCNTs represent an extremely promising medium for surface plasmon enhancement, and present possibly one of the most interesting solutions of developing efficient photonic devices based on collective modes. The study of plasmons in MWCNTs has therefore provided a flurry of research activity. Electron energy-loss spectroscopy (EELS) performed in a scanning transmission electron microscope (STEM) represents a powerful and highly localized tool for probing plasmon excitations in a specimen. Owing to the small electron probe size (<1 nm) and careful definition of the collection angle of the loss signal, EELS offers a spatial resolution of below 1 nm[1,2] that is unrivalled as a bulk analytical tool.

The structure in the EEL spectrum can be ascribed to localized and delocalized states, e.g., interband, intraband, and charge carrier plasmons. Owing to the difference in selection rules, EELS is able to detect plasmon modes,[3] which are not generally detectable by optical methods. Such modes represent the eigenmodes of collective charge density oscillations; at the dipolar limit, the plasmon wave vector is analogous to the photon polarization vector **E**. From the lowering of symmetry from an isotropic electron gas to one restrained to a crystal system, one typically observes a polarization dependence as the primary beam orientation varies with respect to the crystal axes, which is termed optical anisotropy.[4] A further lowering of symmetry would be expected from the nanotube cylindrical geometry.

Graphite and h-BN are often considered as two-dimensional uniaxial solids, and both are optically anisotropic. The graphite π-volume mode resonance originates from the $\pi\rightarrow\pi^{*}$ electric dipole transition, with degeneracy of the π and π^{*} bands allowing excitations at small wave vectors.[4] h-BN, representing a wide band-gap insulator of $E_g\sim 5.9$ eV,[5] also allows excitations at small wave vectors. In both graphite and h-BN, it is the strong directionality of the p_z orbitals perpendicular to the basal planes, the well-known dielectric and optical properties,[6–9] and the ease of availability of nanotube forms that make these crystal forms ideal for investigating polarization effects. Numerous investigations[3,10–12] have demonstrated the orientation dependence of carbon *K*-edge core loss structure. However, very few studies have been performed that scrutinize the optical anisotropy of bulk collective modes;[13–16] angular-resolved secondary-electron emission of graphite is presented in Ref. 17, and reflection EEL studies of graphite are presented in Refs. 6, 7, and 18–20.

Discrete plasmon peaks appear in the EEL spectrum owing to the quantized nature of plasmon modes. An extensive body of literature exists (e.g., from Stéphan's group) concerning the analysis of collective surface modes. EELS studies of these are usually carried out in aloof geometry, for two reasons; firstly, MWCNTs represent quasi-one-dimensional (1D) objects with a large surface-to-volume ratio, and therefore exhibit dominant surface modes. Aloof spectroscopy thus allows direct measurement and isolation of surface modes, without excitation of volume modes. Secondly, extraction of surface modes from EEL spectra acquired in the penetrating geometry is an extremely difficult procedure, since they are obscured by volume modes. However, aloof measurements, due to screening effects, withhold vital information regarding the effect of the nanotube interior (e.g., a dielectric filling), on the graphitic band structure of the wall. In the present contribution, it is demonstrated that a simple model phenomenologically based on primary electron scattering vectors, can be utilized for simulating the π-volume modes of a graphite or h-BN slab: multiwalled nanotubes of >10 nm in diameter present sufficiently small curvature as

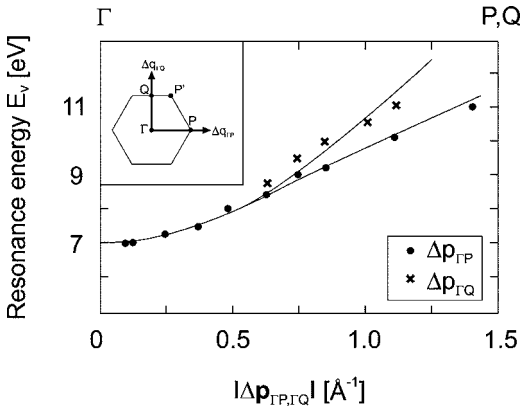

FIG. 1. The positive dispersion of the graphite π-volume mode with $\Delta\mathbf{p}_{\Gamma P,\Gamma Q}$, as measured by angular-resolved EELS. Extracted from Ref. 13. For smaller magnitudes, i.e., $\Delta\mathbf{p}_{\Gamma P,\Gamma Q}<0.5$ Å^{-1}, the anisotropy of the Brillouin zone is imperceptible. For $\Delta\mathbf{p}_{\Gamma P,\Gamma Q}>0.5$ Å^{-1}, the anisotropy of the Brillouin zone results in branching of E_v. Inset: the two-dimensional graphitic and BN Brillouin zone, within which the $\Delta\mathbf{p}_{\Gamma P,\Gamma Q}$ directions are defined.

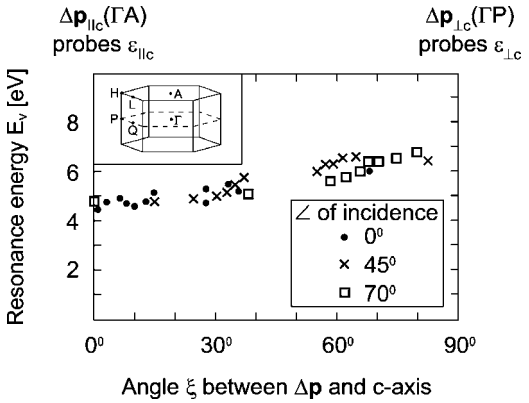

FIG. 2. Variation of the graphite π-volume mode resonance energy with angle of $\Delta\mathbf{p}$ with respect to the c axis, as measured by angular-resolved EELS. Extracted from Ref. 23. Inset: the three-dimensional graphitic and BN Brillouin zone, within which the ΓA and ΓP directions are defined.

to be locally approximated by a slab. The simulated π-volume modes are then utilized to extract volume contributions, from experimental EEL spectra acquired in the penetrating geometry. Finally, it is shown that surface contributions obtained from aloof EELS, and from volume mode-extracted penetrating EELS, exhibit significantly different properties.

II. BAND STRUCTURE AND THE π-VOLUME MODE

Three sources of the graphite or BN volume mode resonance energy modification are now discussed. Momentum transfer from a primary electron to a planar graphite or BN slab can be denoted by $\Delta\mathbf{p}$; dispersive effects within the in-plane component of the dielectric tensor results in a $\Delta\mathbf{p}$ dependence. Since larger $|\Delta\mathbf{p}|$ can reach the edge of the two-dimensional Brillouin zone, the energy of the π-volume mode has a dependence on the magnitude of $|\Delta\mathbf{p}|$. This is termed *wavelength dependence*.[4] The direction of $\Delta\mathbf{p}$ within the two-dimensional Brillouin zone, results in *spatial dispersion*,[4] differing in the ΓP and ΓQ directions. The third source of energy shifting is termed *optical anisotropy*.[4] This arises from the varying angle of $\Delta\mathbf{p}$ with respect to the c axis of graphite or BN, dictating the weighting of transitions associated with the $\mathbf{E}_{\|c}$ and $\mathbf{E}_{\perp c}$ polarizations. The analogous core loss effect, arising from variations of the angle of $\Delta\mathbf{p}$ with respect to the graphitic c axis, thus dictating the final excited state, has been investigated by Rosenberg *et al.*[10] and Leapman *et al.*[3]

The inset of Fig. 1 shows the two-dimensional Brillouin zone of graphite and BN, which are both identical.[21] A momentum transfer in either the ΓP or ΓQ direction (henceforth described using the notation $\Delta\mathbf{p}_{\Gamma P,\Gamma Q}$) with large enough magnitude would theoretically allow excitations from the Γ point to the P and Q points, respectively. The dispersion of the graphitic bulk mode energy E_v as a function of $\Delta\mathbf{p}_{\Gamma P,\Gamma Q}$, is demonstrated in Fig. 1. The band structure-dependent dispersion of E_v is typical of a delocalized state. Owing to the identical two-dimensional Brillouin zone of BN and graphite, a similar dispersion of the BN bulk mode energy on $|\Delta\mathbf{p}_{\Gamma P,\Gamma Q}|$ would be expected. The dispersion occurs as a result of the high density of states between parallel bands shifting to a higher energy with greater $\Delta\mathbf{p}_{\Gamma P,\Gamma Q}$ transfer, i.e., new maxima are formed in the joint density of states (JDOS).[21] Angular-resolved EELS thus probes the dispersive dielectric functions. For smaller magnitudes, i.e., $\Delta\mathbf{p}_{\Gamma P,\Gamma Q}<0.5$ Å^{-1}, the anisotropy of the Brillouin zone is imperceptible, since the difference in length between $\Delta\mathbf{p}_{\Gamma P}$ and $\Delta\mathbf{p}_{\Gamma Q}$ for a momentum transfer in the ΓP or ΓQ direction, is vanishingly small. This results in the value of E_v having a single degenerate value for small momenta transfers. In contrast, for $\Delta\mathbf{p}_{\Gamma P,\Gamma Q}>0.5$ Å^{-1}, the anisotropy of the Brillouin zone results in a lifting of degeneracy, i.e., branching of E_v

Figure 2 details the dependence of E_v, on the angle of a momentum transfer $\Delta\mathbf{p}$, with respect to the c axis of a graphite slab.[15,23] The value of E_v is seen to increase from ~4.6 eV when $\Delta\mathbf{p}$ is in the ΓA direction, to ~7.6 eV when $\Delta\mathbf{p}$ is in the ΓP direction (see inset of Fig. 2, identifying symmetry points within the three-dimensional Brillouin zone), and is invariant with the angle of primary beam incidence to the c axis. Whilst the mosaic spread of BN makes separation of the two polarizations difficult,[24] evidence exists for a similar shift in E_v for a BN slab,[9] as the direction of $\Delta\mathbf{p}$ changes from the ΓA direction to theΓP direction.

Overwhelming evidence exists that this energy shifting of the volume mode is not a "true" dispersion, but rather the different weighting of nearly degenerate and nondegenerate states in the $\mathbf{E}_{\perp c}$ and $\mathbf{E}_{\|c}$ polarizations, which leads to optical anisotropy. Optical anisotropy arises from the varying polarization directions of light, i.e., with the electric vector parallel ($\mathbf{E}_{\|c}$) or perpendicular ($\mathbf{E}_{\perp c}$) to the c axis,[4,22] resulting in variations in the matrix elements. Considering plasmon modes, $\Delta\mathbf{p}_{\|c}$ probes $\varepsilon_{\|c}$, and $\Delta\mathbf{p}_{\perp c}$ probes $\varepsilon_{\perp c}$. Greenaway *et al.*[25] explicitly ascribe the apparent redshift of the graphite volume mode from the ΓP to ΓA direction, to the increasing intensity of a transition at ~4.6 eV, and decreasing intensity of a transition at ~7 eV. Similarly, Hoffman *et al.*[8] ascribe

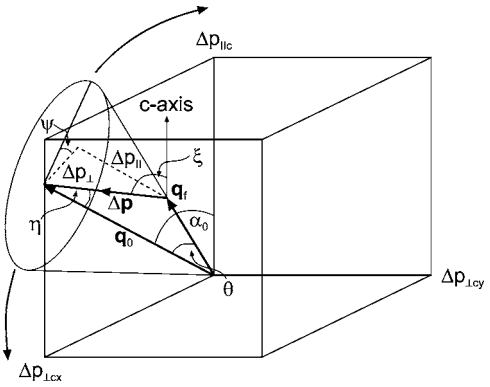

FIG. 3. Scattering kinematics of a primary electron of wave vector q_0, incident on a graphite or BN slab at angle α_0 with respect to the c axis. After the scattering event, the primary electron of wave vector q_f is scattered by angle θ at azimuth ψ, and a plasmon of momentum $\Delta\mathbf{p}$ is excited. For an angle of incidence α_0, the azimuth cone is rotated by α_0 in the plane defined by $\Delta\mathbf{p}_{\|c}$ and $\Delta\mathbf{p}_{\perp cx}$.

the BN peak at 6.85 eV to c-axis dispersion, with this peak increasing in intensity from the ΓP to ΓA direction.

The optical absorption of photons by a medium is described by the imaginary part of the dielectric function, which is related to the JDOS. The transitions in the $\mathbf{E}_{\perp c}(\Delta\mathbf{p}_{\perp c})$ polarization account for structure in the in-plane dielectric function; similarly, transitions in the $\mathbf{E}_{\|c}(\Delta\mathbf{p}_{\|c})$ polarization account for structure in the out-of-plane dielectric function. By considering the kinematics of the scattering process, $\Delta\mathbf{p}$ can be resolved into in-plane and out-of-plane components. This allows one to scrutinize the evolution of optical anisotropy, as the angle of $\Delta\mathbf{p}$ varies with respect to the principal crystal axes.

III. SCATTERING KINEMATICS

A. Volume mode components

Consider the nonconservative excitation of a volume plasmon of momentum $\Delta\mathbf{p}$, in an inelastic collision between a primary electron and a *planar* graphite or BN slab. The momentum transfer $\Delta\mathbf{p}$ can be ascribed to the primary electron being scattered by an angle θ at an azimuth ψ. Figure 3 shows the scattering mechanics of a primary electron possessing momentum $\mathbf{q}_0$, incident on the slab at an angle α_0.

Figure 3 defines $\psi=0$ as the intersection between the azimuth cone and the plane defined by the c axis and the incident beam. $\Delta\mathbf{p}$ can be expressed in terms of parallel and perpendicular components with respect to the *primary beam direction,* whereby, $\Delta\mathbf{p}_\perp=\mathbf{q}_0\theta$ and $\Delta\mathbf{p}_\|=\mathbf{q}_0\theta_E$.[3,23,26] θ_E represents the most likely scattering angle of the primary beam.[27] Assuming dimensional effects[28–30] are neglected, the plasmon wave vector $\Delta\mathbf{p}$ can also be resolved into components in the direction of the unitary basis vectors $\mathbf{i}$, $\mathbf{j}$, $\mathbf{k}$, representing vector components in an orthogonal coordinate system. Aligning $\mathbf{k}$ with the [0001] direction of the hexagonal crystal, the direction of $\mathbf{k}$ is then defined as the ΓA direction, with $\mathbf{j}$ and $\mathbf{k}$ defined as orthogonal directions in the basal plane. The components of $\Delta\mathbf{p}$ are then given by[27,31–34]

$$\begin{matrix}\mathbf{i}\\ \mathbf{j}\\ \mathbf{k}\end{matrix}\begin{bmatrix}\Delta p_x\\ \Delta p_y\\ \Delta p_z\end{bmatrix}=\begin{bmatrix}\mathbf{q}_0\theta_E\sin\alpha_0-\mathbf{q}_0\theta\cos\psi\cos\alpha_0\\ \mathbf{q}_0\,\theta\sin\psi\\ \mathbf{q}_0\theta_E\cos\alpha_0+\mathbf{q}_0\theta\sin\alpha_0\cos\psi\end{bmatrix}. \quad (1)$$

The plasmon vector $\Delta\mathbf{p}$ is then defined with respect to the c axis, which is rotated relative to the primary beam direction by α_0. The magnitude of the in-plane and out-of-plane components of the volume plasmon wave vector can thus be represented by

$$\frac{d^2|\Delta\mathbf{q}_{\perp c}|}{d\theta d\psi}=\sqrt{\mathbf{i}[\Delta p_x]^2+\mathbf{j}[\Delta p_y]^2} \quad (2)$$

and

$$\frac{d^2|\Delta\mathbf{q}_{\|c}|}{d\theta d\psi}=\sqrt{\mathbf{k}[\Delta p_z]^2}. \quad (3)$$

$\Delta\mathbf{q}$ represents the *total effective* plasmon wave vector; the volume mode loss function is largely determined by the in-plane and out-of-plane components $\Delta\mathbf{q}_{\perp c}$ and $\Delta\mathbf{q}_{\|c}$, each weighting the in-plane and out-of-plane dielectric tensor components, respectively. It is now clearly evident how optical anisotropy dictates the nature of the EEL spectrum. Equation (1) demonstrates that components of $\Delta\mathbf{p}$ are a function of the incidence angle, scattering angle, and azimuth; $\Delta\mathbf{q}$, $\Delta\mathbf{q}_{\perp c}$, and $\Delta\mathbf{q}_{\|c}$ are henceforth written as functions of α_0, θ, and ψ. The phenomenological technique of resolving $\Delta\mathbf{q}(\alpha_0,\theta,\psi)$ into in-plane and out-of-plane components is identical to that utilized by Leapman *et al.*[3] in order to study states polarized parallel and perpendicular to the c axis, for core losses of a graphite slab. Further discussion of such polarized core loss states is provided in Rosenberg *et al.*[10]

It should be noted that the most likely propagation angle of the $d|\Delta\mathbf{q}(\alpha_0,\theta_E,\psi)|/d\psi$ vectors (easily calculated by adding Eqs. (2) and (3) in quadrature, and by assuming $\theta=\theta_E$), is at $\eta_E=45°$ to the primary beam direction at all azimuths; for *any* angle of incidence a volume plasmon "cone" is thus formed. This cone consists of $d|\Delta\mathbf{q}(\alpha_0,\theta_E,\psi)|/d\psi$ vectors of identical length 6.9×10^{-3} Å^{-1}, assuming a primary beam energy of 100 keV, and a π-volume mode energy of ~6.75 eV. Figure 1 shows a momentum transfer $\Delta\mathbf{p}\gg6.9\times10^{-3}$ Å^{-1} is required to reach the edges of the Brillouin zone; thus the limit $d|\Delta\mathbf{q}(\alpha_0,\theta_E,\psi)|/d\psi\to0$ probes energy bands, only in the immediate vicinity of the Γ point. This means energy shifting of the π-volume mode *cannot* be attributed to dispersive effects of higher $d|\Delta\mathbf{q}_{\perp c}(\alpha_0,\theta_E,\psi)|/d\psi$ values. The effects of spatial anisotropy can thus be neglected, since $d|\Delta\mathbf{q}(\alpha_0,\theta_E,\psi)|/d\psi$ is not large enough to lift degeneracy (the branching point of Fig. 1). This results in a vanishingly small dispersion of the volume mode energy, as the orientation of the beam varies from the ΓP direction to the ΓQ direction.

B. The critical wave vector

The critical wave vector $\mathbf{q}_c$ represents the maximum threshold momentum transfer, for collective excitations in a

plasma.[35] Beyond $\mathbf{q}_c$, the plasmon is unstable and decays into a single electron excitation. $\mathbf{q}_c$ can be assigned to a critical angle θ_c; only electrons scattered by an angle $<\theta_c$ contribute to the collected energy-loss function.[36] In order to estimate the maximum threshold $\mathbf{q}_c$, one can assume that in an inelastic collision, momentum is transferred to the fastest possible plasma electrons, i.e., those having the Fermi velocity. Values of $\Delta\bar{E}=6.75$ eV (representing a mean value of the experimentally measured graphite π-volume mode loss function resonance energy) and $v_F=8.11\times10^5$ ms^{-1},[37] provide[36]

$$\theta_c \approx \frac{\Delta\bar{E}}{2\pi\hbar\, v_F \mathbf{q}_0} = 1.1\times10^{-3}\ \text{rad}. \tag{4}$$

This calculated value of θ_c corresponds to a value of $\mathbf{q}_c \sim \mathbf{q}_0\theta_c = 1$ nm^{-1}, consistent with values provided in literature ranging from $\mathbf{q}_c \sim 1$ nm^{-1} to $\mathbf{q}_c \sim 10$ nm^{-1}.[37,38] The spectrometer collector aperture (of semiangle $\beta=3.4\times10^{-3}$ rad) samples a restricted region of $\mathbf{k}$ space; electrons are collected primarily from the restricted $\mathbf{k}$-space region possessing a high density of states. However, since $\theta_c \ll \beta$, *all* possible values of $|\Delta\mathbf{q}(\alpha_0,\theta,\psi)|/d\theta d\psi$ can be assumed to be admitted by the aperture. The volume mode loss function consists of the $\Delta\mathbf{q}_{\perp c}(\alpha_0,\theta,\psi)$ and $\Delta\mathbf{q}_{\parallel c}(\alpha_0,\theta,\psi)$ components weighting the in-plane and out-of-plane dielectric tensor components, respectively. For simulation of realistic spectra, the double integration of Eqs. (2) and (3) is required, over possible values of θ and ψ, namely from $\theta=0$ to $\theta=\theta_c$, and $\psi=0$ to $\psi=2\pi$.

In order to demonstrate the effect of the relative weighting of $\Delta\mathbf{q}_{\perp c}(\alpha_0,\theta,\psi)$ and $\Delta\mathbf{q}_{\parallel c}(\alpha_0,\theta,\psi)$ on experimentally-measured[9,39] π-volume mode loss function parameters, a full calculation of the π-volume mode EEL probability for a graphite and BN slab is performed in Sec. V. Firstly, corrections to the slab thickness and angle of beam incidence on the slab, arising from the cylindrical nanotube geometry, must be considered.

IV. CYLINDRICAL SYMMETRY

A. The volume mode angular distribution

The angle ξ between the volume mode wave vector and c axis, and the angle η between the volume mode wave vector and $\mathbf{q}_0$, are defined in Fig. 3. It is a quantity dependent on ξ that largely dictates the parameters of the volume mode loss function, namely the relative weighting of the total effective in-plane and out-of-plane volume mode components. Calculating the angle ξ provides some interesting results, and predicts the existence of cylindrical anisotropy. ξ may be calculated from[40]

$$\cos\xi = |\cos\eta(\theta)\cos\alpha_0 - \sin\eta(\theta)\sin\alpha_0\cos\psi|. \tag{5}$$

From Eq. (5), it is evident that ξ has a dependency on the incidence angle, scattering angle, and azimuth; ξ is henceforth written as $\xi(\alpha_0,\theta,\psi)$. It has already been seen at the condition $\theta=\theta_E$, that $\Delta\mathbf{p}_\perp=\Delta\mathbf{p}_\parallel=\mathbf{q}_0\theta_E$, thus it follows that $\eta_E=45°$, identified as the most likely angle between the volume mode and $\mathbf{q}_0$. At this condition, Eq. (5) can be reduced to

$$\cos\xi(\alpha_0,\theta_E,\psi) = \frac{1}{\sqrt{2}}|\cos\alpha_0 - \sin\alpha_0\cos\psi|. \tag{6}$$

Equation (6) allows one to physically interpret a complex three-dimensional problem. For example, solving Eq. (6) for $\xi(\alpha_0=65°,\theta_E,\psi)=80°$, four solutions are seen to occur at $\psi\sim42°$, 80°, 280°, and 315°. In contrast, for $\xi(\alpha_0=65°,\theta_E,\psi)=30°$, only two solutions occur at $\psi\sim150°$ and 210°. This demonstrates for a given angle of incidence α_0, the probability of the volume mode propagating at a given angle $\xi(\alpha_0,\theta_E,\psi)$ can vary. Equation (6) therefore predicts asymmetry of the volume mode wave-vector angular distribution. The second prediction is that as the angle of incidence α_0 changes, this asymmetry will evolve.

When the beam penetrates a multiwalled nanotube, due to the continuous change in angle of incidence at each layer,[41] predicting the volume mode angular distribution becomes nontrivial. For an angle of incidence α_i on the ith nanotube wall, there is an angular distribution $f[\xi(\alpha_i,\theta,\psi)]$. For an angle of incidence α_{i+1} on the $i+1$th wall, there is an angular distribution $f[\xi(\alpha_{i+1},\theta,\psi)]$. Assuming a nonzero impact parameter b, it follows that $\alpha_{i+1}\neq\alpha_i$, thus the distribution $f[\xi(\alpha_{i+1},\theta,\psi)]\neq f[\xi(\alpha_i,\theta,\psi)]$. Using Eq. (6), one can calculate the frequency distribution of the angle between the volume mode wave vector and the c axis, for discrete azimuth values ψ_j. Assuming the beam penetrates n layers, and summing the angular frequencies $f[\xi(\alpha_i,\theta_E,\psi_j)]$ for each wall penetrated,

$$f[\xi(\alpha,\theta_E,\psi)] = \sum_{i=1}^{i=n}\sum_{j=1°}^{j=360°} f[\xi(\alpha_i,\theta_E,\psi_j)]. \tag{7}$$

Equation (7) thus provides the volume mode wave-vector angular distribution for a multiwalled nanotube. Simulated angular distributions calculated using Eq. (7), are shown in Fig. 4.

The ratio between the inner nanotube wall radius $r_{i=1}$ and outer nanotube wall radius $r_{i=n}$ is henceforth denoted by r_1/r_2, following the usual nomenclature utilized in literature. The parameters $r_1(r_2)$ thus represent the inner (outer) nanotube wall radii. When n is small, $r_1/r_2\to1$ denotes a thin nanotube; when n is large, $r_1/r_2\to0$ denotes a thick nanotube. Specific values of r_1/r_2 were chosen for simulation in Fig. 4, because they correspond to the parameters of nanotubes, from which experimental data are later scrutinized. When the impact parameter becomes larger than the nanotube inner wall radius r_1, the number of walls penetrated by a primary electron decreases. This has been accounted for in the simulations of Fig. 4.

At $b=0$, the volume mode has an invariant angle to the c axis for each wall, as seen in Fig. 4, resulting in the minimum angular width. For $0<b<5r_2/7$, the volume mode has a wider range of angles to the c axis, and for $b>6r_2/7$, the angular width decreases. For the thin nanotube ($r_1/r_2=0.97$), the frequency of each angle is less than that of the thick nanotube ($r_1/r_2=0.29$) at a given b. This arises from the fewer walls being penetrated in the thinner tube. Furthermore, for a given impact parameter, the angular width is

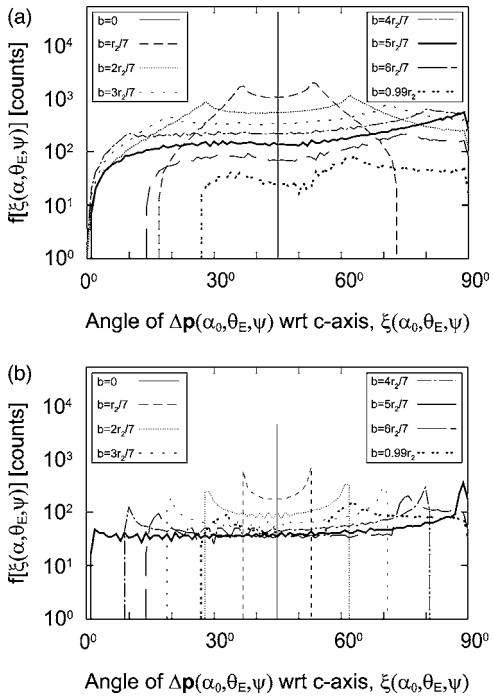

FIG. 4. The frequency distribution of the angle between the volume mode wave vector and the c axis, for a multiwalled nanotube, at discrete azimuth values, for $b=0$ to $b=0.99\ r_2$. (a) Thick nanotube, with parameters $r_1=15$ nm, $r_2=51$ nm, and $r_1/r_2=0.29$. (b) Thin nanotube, with parameters $r_1=117$ nm, $r_2=121$ nm, and $r_1/r_2=0.97$.

consistently greater for the thicker tube than for the thinner tube. This effect arises from the larger range of angles of incidence of the primary beam, on each layer of a nanotube possessing a larger number of walls. This effect is termed cylindrical anisotropy, which is now quantified.

B. Calculation of cylindrical anisotropy

Consider a multiwalled nanotube of inner (outer) radii r_1 (r_2), and [0001] spacing d, which is penetrated by an electron beam at an impact parameter b, where $b\neq 0$. In the cylindrical geometry, the angle of incidence of the beam on each layer is a function of the impact parameter. Assuming i is the layer number, a series of incidence angles $\alpha_{i=1}(b)\ldots\alpha_{i=n}(b)$ of the beam on the ith layer occurs, which is given by

$$\alpha_i(b)=\arcsin\left[\frac{b}{r_2-(i-1)d}\right]. \tag{8}$$

The direction g can be defined as the direction orthogonal to both the nanotube axis and the impact parameter direction b; the intersection height g_i of the primary beam on the ith nanotube layer is defined in Fig. 5. The abscissa coordinate g, of the point of penetration of the primary beam on each nanotube layer, can be calculated from

$$g_i(\alpha_i,b)=\frac{b}{\tan\alpha_i(b)}. \tag{9}$$

The number of walls *penetrated* by the beam, herein termed

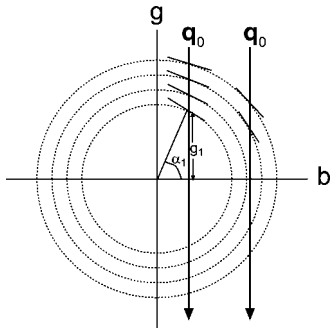

FIG. 5. Schematic representation of a primary beam q_0 incident on a multiwalled nanotube for both $b<r_1$ and $b>r_1$. Each layer is represented as a Dirac delta function. Locally the nanotube walls are approximated as a planar slab. In this approximation, both the varying angle of incidence of the primary beam on each nanotube layer, and the reduction in number of walls penetrated for $b>r_1$, are preserved. For a given b, the beam intersects each layer at a given height g_i. The intersection height g_1 of the beam on the first layer is identified for $b<r_1$.

$n(b)$, is not necessarily the same as the number of walls possessed by the nanotube. Calculating $n(b)$ for the two regions $0<b<r_1$ and $r_1<b<r_2$, provides

$$n(b)=2\left[\left(\frac{r_2-r_1}{d}\right)\Theta(b)-\left(\frac{b-r_1}{d}\right)\Theta(b-r_1)\right]. \tag{10}$$

The Θ term represents the Heaviside step function. Figure 6 demonstrates the continuous change in angle of incidence of the beam on each layer, for both thick and thin multiwalled nanotubes. The region $b>r_1$ with undefined angles of incidence corresponds to the reduction in the number of walls penetrated by the primary beam. One can immediately see for a zero impact parameter, the angle of incidence has an invariant value of 0° at each layer. At an impact parameter equal to r_2, there is a grazing angle of incidence at the final remaining outermost layer. Consider a beam incident on a nanotube; let $\Delta\alpha(b)$ be the range of angles of incidence, at an impact parameter b, from the outermost layer $\alpha_{i=n}(b)$ to the innermost layer $\alpha_{i=1}(b)$. For a nanotube of parameter $r_1/r_2\rightarrow 0$, a small impact parameter δb results in a large $\Delta\alpha(b)$ range; at $b=r_1$, Fig. 6(a) shows $\Delta\alpha(b)\rightarrow 90°$ for a nanotube with $r_1/r_2=0.1$. In contrast, for $r_1/r_2\rightarrow 1$, $\Delta\alpha(b)$ is nearly invariant at any impact parameter, e.g., at $b=r_1$ in Fig. 6(b), $\Delta\alpha(b)<10°$.

In the following section, it is seen that accounting for the changing values of α_i for each layer is required, in order to accurately simulate volume mode parameters.

V. SIMULATED VOLUME MODES

A. Dielectric tensor

The polarization response of a nanotube to an external field is determined by the complex dielectric tensor; the final step in simulating volume modes is therefore to weight the dielectric tensor with the relevant components of $\Delta\mathbf{q}(\alpha_i,\theta,\psi)$.

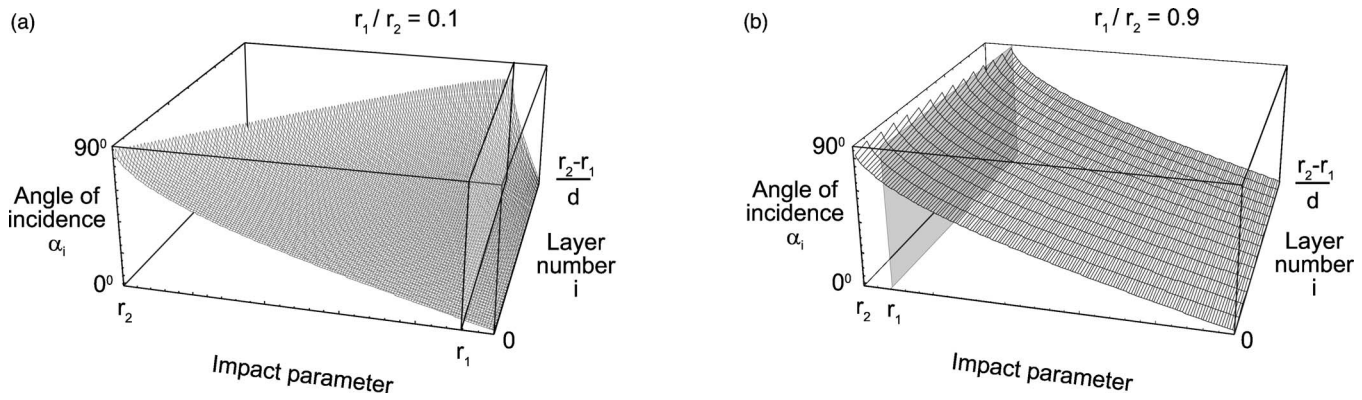

FIG. 6. The continuous change in angle of incidence of the primary beam on each multiwalled nanotube layer. (a) A thick nanotube, and (b) a thin nanotube.

The dielectric constants of graphite and hexagonal BN have the form of a 3×3 tensor. **i**, **j**, **k** represent the unitary basis vectors in an orthogonal coordinate system. It can be shown that $\varepsilon_{ij}=\varepsilon_{ji}$ for $j\neq i$.[42,43] Having aligned **k** with the [0001] direction,[42] the nine components of the tensor reduce to the three components ε_{ii}, ε_{jj}, and ε_{kk}. Owing to $|\Delta\mathbf{p}|\rightarrow0$, i.e., the branching point of Fig. 1 not being attained, it can be approximated that ε_{ii} and ε_{jj} are degenerate, thus $\varepsilon_{\perp cx}=\varepsilon_{\perp cy}$; it can further be approximated that the optical limit has been reached. The in-plane and out-of-plane components of the dielectric tensor for each polarization are then described by the $\varepsilon_{\perp c}(\omega)$ and $\varepsilon_{\parallel c}(\omega)$, respectively. The graphite tensor components were taken from published optical data,[44,45] and those for BN were taken from published inelastic electron scattering data.[9] Expressions for the dielectric functions were then derived by fitting Drude-Lorentz functions to the data. The modeled and experimentally measured dielectric functions are detailed in Fig. 7.

B. Classical dielectric model

Models approximating graphite or BN as an isotropic medium,[46] or approximating the nanotube forms as being

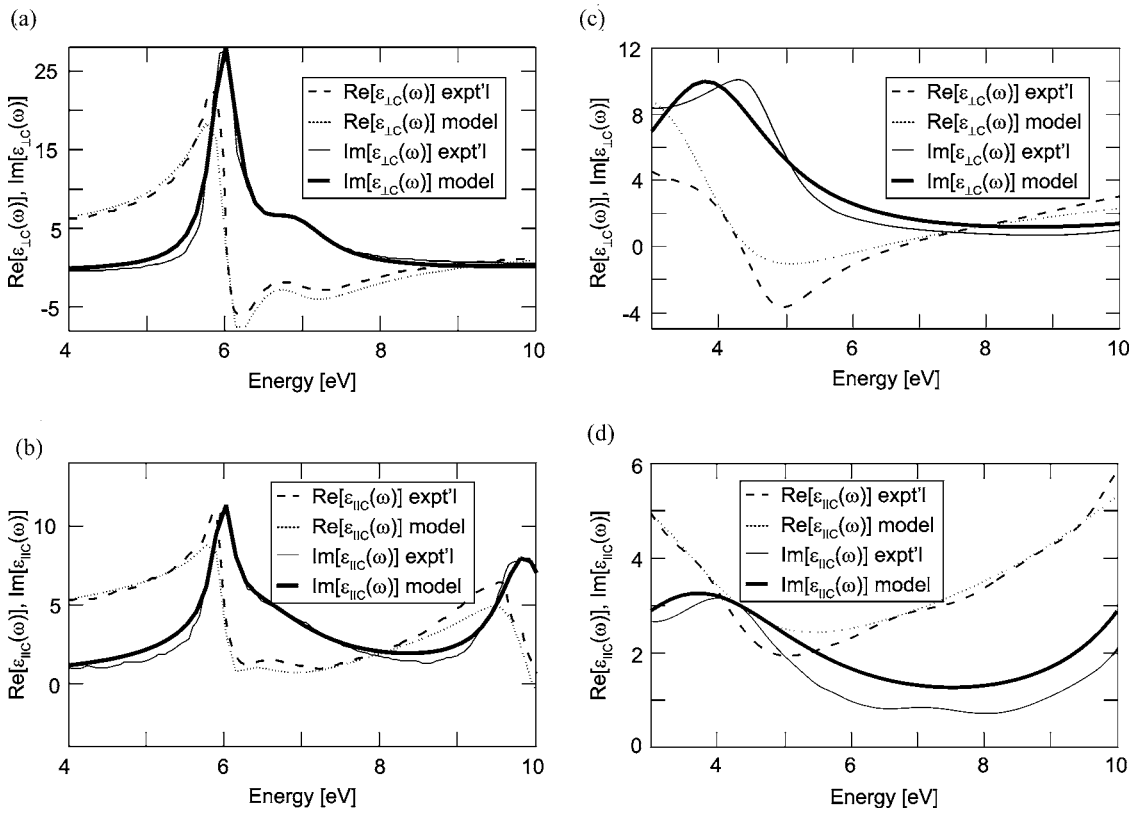

FIG. 7. The graphite and BN dielectric functions for the $\mathbf{E}_{\parallel c}$ and $\mathbf{E}_{\perp c}$ polarizations, modeled using a Drude-Lorentz profile. BN experimental data has been extracted from Ref. 9, graphite experimental data has been extracted from Refs. 44 and 45. (a) and (b), BN. (c) and (d), graphite.

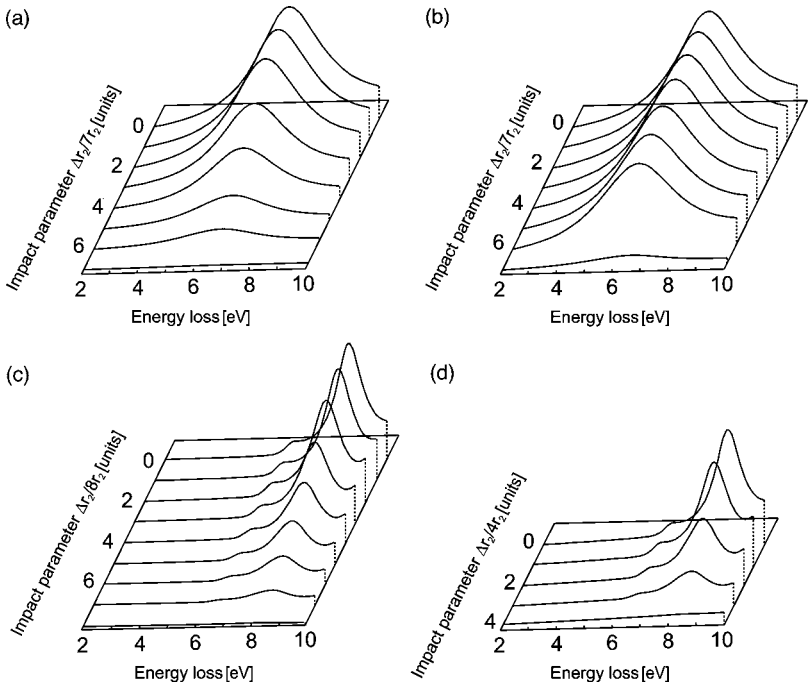

FIG. 8. Simulations of π-volume mode for various b, calculated using Eq. (13). The intensity has been normalized at $b=0$. (a) Thick MWCNT, $r_1=15$ nm, $r_2=51$ nm, $r_1/r_2=0.29$. (b) Thin MWCNT, $r_1=117$ nm, $r_2=121$ nm, $r_1/r_2=0.97$. (c) MWBNNT, $r_1=19$ nm, $r_2=71$ nm, $r_1/r_2=0.26$. (d) MWBNNT, $r_1=11$ nm, $r_2=35$ nm, $r_1/r_2=0.31$.

without a cavity,[32] are clearly inadequate for an accurate simulation of volume modes. Various other inadequate approaches also exist.[47,48] For simulations in the present contribution, a classical nonrelativistic electrodynamic formalism for a planar slab was utilized, which has in the past been used with considerable success in explaining EEL features. This approach is now corrected for the cylindrical geometry.

Integrating over possible scattering angles θ and azimuths ψ, the volume mode excitation probability, per unit path length of the primary electron in a graphite or BN slab, is given by[32]

$$\frac{d^2P^{vol}(\omega,\alpha_0,\theta,\psi)}{d\omega dg} = \frac{e^2}{4\pi^3 v^2 \varepsilon_0 \hbar}\int_0^{2\pi}\int_0^{\theta_c}\theta \times \mathrm{Im}\left[\frac{-\mathbf{q}_0^2}{\Delta\mathbf{p}_{\perp c}^2(\alpha_0,\theta,\psi)\varepsilon_{\perp c}(\omega)+\Delta\mathbf{p}_{\|c}^2(\alpha_0,\theta,\psi)\varepsilon_{\|c}(\omega)}\right] \times d\theta d\psi. \quad (11)$$

In order to apply this model to the cylindrical nanotube geometry, various studies[32,49] have utilized the angle between the primary beam and the *outermost* nanotube wall, to provide a value of α_0. Figure 6 clearly demonstrates that the angle between the primary beam and each nanotube wall is not uniform. We now consider avoiding this approximation. Treating each layer as discrete, in order to account for cylindrical anisotropy via the changing angles of incidence on each layer, Eq. (11) can be corrected to

$$\frac{d^2P^{vol}(\omega,\alpha_i,\theta,\psi,b)}{d\omega dg} = \frac{e^2}{4\pi^3 v^2 \varepsilon_0 \hbar}\int_0^{2\pi}\int_0^{\theta_c}\theta \times \mathrm{Im}\left[\frac{-\mathbf{q}_0^2}{\Delta\mathbf{p}_{\perp c}^2(\alpha_i,\theta,\psi,b)\varepsilon_{\perp c}(\omega)+\Delta\mathbf{p}_{\|c}^2(\alpha_i,\theta,\psi,b)\varepsilon_{\|c}(\omega)}\right] \times d\theta d\psi. \quad (12)$$

Equation (12) can be considered to represent the volume plasmon excitation probability for the ith nanotube layer. The volume plasmon excitation probability arising from all the nanotube layers, is therefore provided by Eq. (12) summed over the number of layers penetrated by the primary beam, thus,

$$\frac{dP^{vol}(\omega,\alpha_i,\theta,\psi,b)}{d\omega} = \frac{e^2}{4\pi^3 v^2 \varepsilon_0 \hbar} 2\sum_{i=1}^{n(b)} \delta[g-g_i(\alpha_i,b)] \times \int_0^{2\pi}\int_0^{\theta_c}\theta \times \mathrm{Im}\left[\frac{-\mathbf{q}_0^2}{\Delta\mathbf{p}_{\perp c}^2(\alpha_i,\theta,\psi,b)\varepsilon_{\perp c}(\omega)+\Delta\mathbf{p}_{\|c}^2(\alpha_i,\theta,\psi,b)\varepsilon_{\|c}(\omega)}\right] \times d\theta d\psi. \quad (13)$$

The delta function in Eq. (13) forces the double integral to be evaluated only at $g=g_i(\alpha_i,b)$, corresponding to the intersection of the beam at each nanotube wall; for $g\neq g_i(\alpha_i,b)$, the double integral is zero.

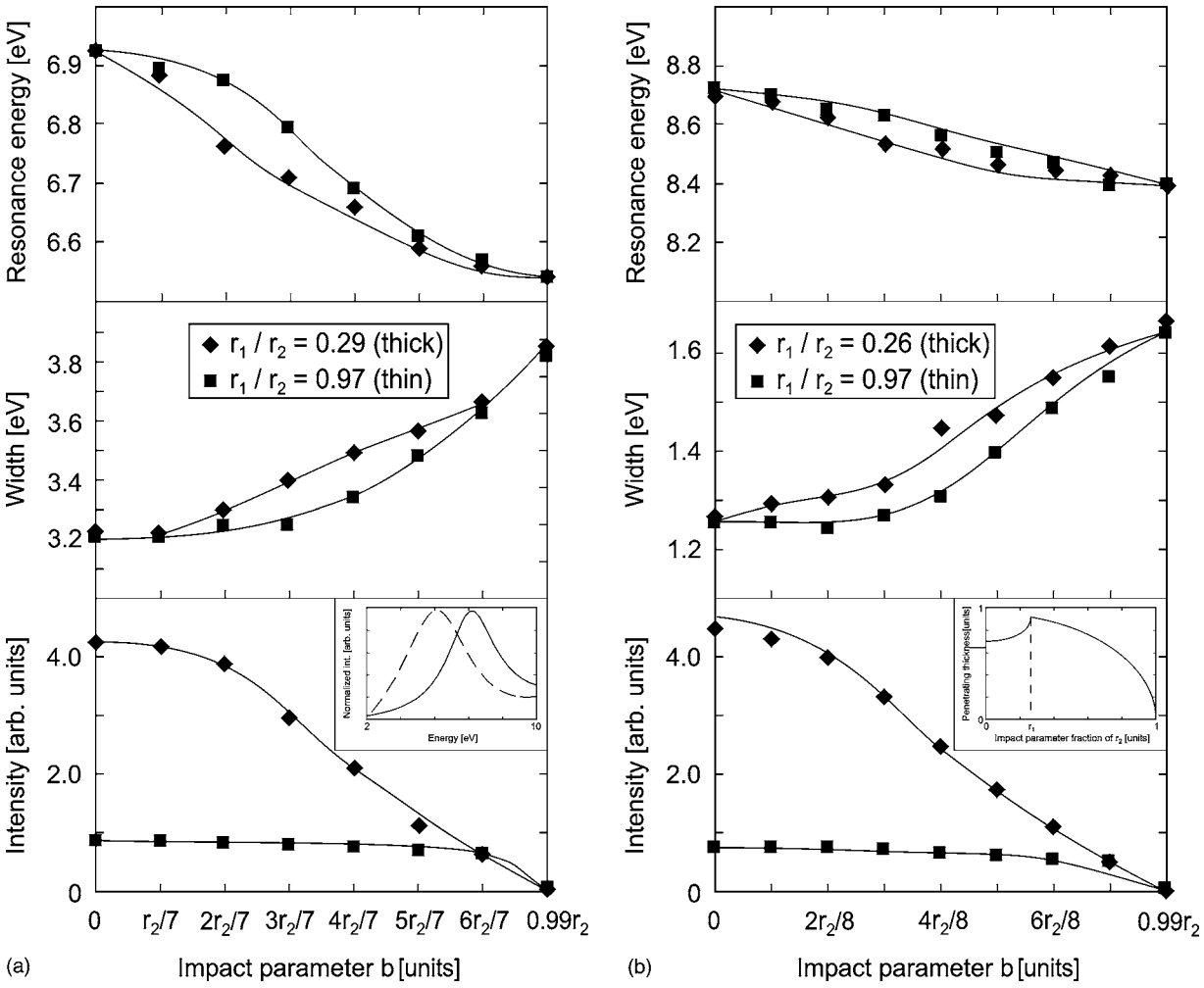

FIG. 9. Parameters of the spectra of Fig. 8, as a function of impact parameter. (a) MWCNT. (b) MWBNNT (the parameters represent those of the Gaussian peak fitted to the resonance appearing in the simulated spectrum at ~8.5 eV). Inset in (a) Simulated π-volume modes for the thick MWCNT, assuming integration limits $\theta=0$ to $\theta=0.01\theta_E$. $b=0$ (dashed line), $b=0.99\ r_2$ (solid line). Inset in (b) The path length of a primary beam at impact parameter b with respect to the cylinder axis, in a cylinder of parameters inner (outer) radii r_1, r_2. The path length attains a maximum value at $b=r_2$.

C. Simulated volume mode parameters

Simulated MWCNT and MWBNNT π-volume modes are illustrated in Fig. 8. In these simulations, a maximum impact parameter of $b=0.99r_2$ was used, as opposed to $b=r_2$, in order to avoid a zero penetrating thickness. Detailed analyses of these spectra, concerning width, energy and intensity, are provided in Fig. 9. The trends in width, resonance energy, and intensity variation of simulated π-volume modes with b are clearly generic, applying to both MWCNTs and MWBNNTs. With regard to graphite, Fig. 2 details the π-volume mode loss function maximum at ~7 eV for the in-plane geometry and ~5 eV for the out-of-plane geometry; at $b=0$, the resonance energy of ~6.9 eV thus suggests the dominance in weighting of $\varepsilon_{\perp c}$ over $\varepsilon_{\parallel c}$. This contrasts with normal incidence EELS typically utilized to measure $\varepsilon_{\parallel c}$ for planar graphite slabs.[21,40] The reason for the present simulations at $b=0$ being dominated by the weighting of $\varepsilon_{\perp c}$, is ascribed to the integration in Eq. (13) of the primary electron scattering angle, from $\theta=0$ to $\theta=\theta_c$. Physically, these integration limits allow high angle scattering to contribute to the π-volume mode loss function; high angle scattering results in plasmon wave vectors nearly perpendicular to the c axis, which tend to weight $\varepsilon_{\perp c}$.

In the inset of Fig. 9(a), the effect of restricting scattering to small θ for the π-volume mode simulations is demonstrated. Setting the integration limits from $\theta=0$ to $\theta \ll \theta_E$ reproduces measurements by angular-resolved EELS as detailed in Fig. 2; at $b=0$, the π-volume mode loss function is dominated by the weighting of $\varepsilon_{\parallel c}$, resulting in a resonance energy of ~5 eV, at $b=0.99r_2$, the π-volume mode loss function is dominated by the weighting of $\varepsilon_{\perp c}$, resulting in a resonance energy of ~7 eV. However, unless a very small collector aperture is used, a measured (not angular-resolved) EEL spectrum for a graphitic or BN material will always contain contributions from both $\varepsilon_{\perp c}$ and $\varepsilon_{\parallel c}$, whereas angular-resolved EELS is able to isolate contributions from either $\varepsilon_{\perp c}$ or $\varepsilon_{\parallel c}$.

Owing to contributions of both the in-plane and out-of plane dielectric tensor components to the π-volume mode,

when angular-resolved EELS is not used, it is an oversimplification to assign the π-volume mode solely to $\varepsilon_{\perp c}$ (e.g., see Ref. 50). As b increases, an increased weighting of $\varepsilon_{\|c}$ with respect to $\varepsilon_{\perp c}$ occurs, resulting in an increasing weighting of lower energy features associated with $\varepsilon_{\|c}$. Figures 9(a) and 9(b) therefore show an *apparent* redshift of the resonance energy with b. Nevertheless, simulations appearing in literature of the π-volume mode redshift with b, of MWCNTs or multiwalled carbon nanospheres, must be treated with caution. Reference 32 details simulated redshifting of the *composite* π*-peak* (i.e., containing both bulk and surface contributions) from 7 eV at $b=0$, to 6 eV at $b=0.99r_2$ for a carbon nanosphere of radius 5 nm, utilizing a classical dielectric response model. Whilst this redshift is generally consistent with the present MWCNT simulations, in addition to cylindrical anisotropy not being accounted for, this redshift may arise simply from the increasing surface contributions with b.

Marinopoulos *et al.*[16] detail *ab initio* calculations of the graphite EEL function, within the time-dependent density-functional theory framework. In their study, the influence of local field effect (LFE) was deduced. With regard to the π plasmon, for $\mathbf{p}_{\perp c}$, the LFE was seen to have a vanishingly small effect, and as ξ decreased, the LFE was seen to increase. Comparing calculated EEL functions for $\mathbf{p}_{\|c}$ both with and without the LFE accounted for, better agreement with experimental spectra was attained when the LFE was included. Whilst in the present contribution, loss function models are based on experimentally measured response functions, more sophisticated carbon nanotube EELS models calculated using the time-dependent density-functional theory approach[16] mentioned above, would thus seem to require the LFE to be accounted for, in order to accurately explain features in absorption spectra.[51]

With regard to the present simulated line widths, the increase with b can be ascribed purely to the increasing weighting of features associated with $\varepsilon_{\|c}$, compared to those associated with $\varepsilon_{\perp c}$. It is noted that the present simulated line widths are significantly smaller than those of MWCNTs measured in Ref. 52 using EELS. We strongly suspect this is due to the π peaks of Ref. 52 containing surface contributions.

For both the thick and thin nanotubes at $b=0.99r_2$, the ratio of the weighting of the lower energy features associated with $\varepsilon_{\|c}$ to the higher energy features associated with $\varepsilon_{\perp c}$ is identical, since the path length of the primary electron through both nanotubes is nearly identical, and the angle of incidence is grazing. This results in precisely the same resonance energy and line width at $b=0.99r_2$ for both nanotubes. For both the thick and thin nanotubes at $b=0$, the weighting of $\varepsilon_{\|c}$ is vanishingly small, resulting in precisely the same resonance energy and line width at $b=0$ for both nanotubes. The identical resonance energy at $b=0$ for both the thicker and thinner nanotubes is consistent with EEL measurements of thick and thin multiwalled carbon nanospheres provided in literature.[30] For a given b where $b\neq 0$ and $b\neq 0.99r_2$, the thicker nanotube has a larger weighting of $\varepsilon_{\|c}$ with respect to $\varepsilon_{\perp c}$, owing to greater thickness. This results in the π-volume mode width of a thicker nanotube being consistently larger than that of a thinner nanotube, and the resonance energy of the π-volume mode being consistently lower for a thicker nanotube than that of a thinner nanotube.

Literature suggests the π-volume plasmon is significantly affected by the number of layers of a multiwalled nanotube.[53] The intensity of the simulated π-volume modes are seen to have a maximum value at $b=0$, tending to zero at $b=0.99r_2$. This is consistent with trends detailed in literature.[30,52,54,55] In contrast, a cylinder made from a quasi-free electron metal would have the greatest volume mode intensity, when the path penetrated by the probe electron is greatest (i.e., at $b=r_1$). This effect would be resolvable for a large cylinder, and is illustrated in the inset of Fig. 9(b). This discrepancy has presented a puzzle that has not been resolved in literature.[55] Considering the π-volume mode intensity for the in-plane geometry is very much greater than that for the out-of-plane geometry, and that $\varepsilon_{\perp c}$ has the greatest (least) weighting with respect to $\varepsilon_{\|c}$ at $b=0$ ($b=0.99r_2$), π-volume modes of a multiwalled nanotube are most intense at $b=0$, and least intense at grazing incidence. The decrease in the number of walls penetrated for $b>r_1$, represents an additional effect contributing to the decrease in intensity with b. Interestingly, an accurate value of the graphite critical wave vector is not known. However, from the present simulations correctly reproducing the experimentally observed volume mode intensity evolution[55] with b, one can infer the actual graphite critical wave vector value is indeed between $\mathbf{q}_c=1\ \mathrm{nm}^{-1}$ and $\mathbf{q}_c=10\ \mathrm{nm}^{-1}$, consistent with other estimates.[37,46]

D. Dimensional changes

The volume mode model presented so far neglects the possibility of dimensionality changes of the π-volume mode.[28–30] Such dimensionality changes are predicted to enable a MWCNT π-volume mode to disperse at small $\Delta\mathbf{p}$ magnitudes, dependent on the number of walls possessed by the MWCNT.

Reference 56 investigates the resonance energy dependence of $(\pi+\sigma)$-volume and $(\pi+\sigma)$-surface modes with the number of walls possessed by a MWCNT. EEL spectra were acquired at non-normal incidence ($b\neq 0$) positions with respect to the MWCNT axes, in MWCNTs possessing from 12 to 29 walls. No size dependence of the $(\pi+\sigma)$-volume or $(\pi+\sigma)$-surface mode resonance energy was evident. However, one cannot draw firm conclusions from this observation, since owing to $b\neq 0$, volume contributions were obscured by surface contributions.

Eliminating the obscuring effect of surface contributions, Ref. 30 presents EEL spectra acquired at normal incidence ($b=0$) with respect to multiwall carbon nanospheres, with outer diameters ranging from 5.6 nm to 14.5 nm. For both π- and $(\pi+\sigma)$-volume modes, no size dependence of the resonance energy was evident. One can thus reasonably infer that MWCNTs of down to $\sim$5 nm in thickness, represent the size regime where dimensionality changes are not evident. Only very near the single shell limit ($r_2-r_1\ll 5$ nm) will π-volume modes be suppressed, with a consequent reduction in resonance energy.[57]

VI. EXTRACTION OF VOLUME CONTRIBUTIONS FROM EXPERIMENTAL SPECTRA

For the remainder of this contribution, in order to test the volume mode model, π-volume contributions are extracted

from experimental MWCNT spectra acquired in the penetrating mode for the entire range from $b=0$ to $b=0.99r_2$. Finally, as a demonstration of the practical value of the model, a straightforward example of resolving MWCNT coupled π-surface features with modified eigenenergies owing to the presence of a dielectric filling is performed, which up until present has not been experimentally validated.

A. Experimental details

EEL spectra were acquired utilizing a CCD detector-based Gatan Enfina system attached to a dedicated VG-HB601 scanning transmission electron microscope (STEM). The Enfina system enables EEL measurements to be performed in "spectrum imaging mode,"[58–61] allowing one to acquire both penetrating and aloof spectra within the same spectrum image. The STEM was equipped with a 100 keV cold field emission source, providing a probe size of <1 nm. The high real-space resolution of the EEL analysis prevented "averaging" of orientations of the primary beam, with respect to the planes. Utilizing a dispersion of 0.01 eV/ch provided a zero-loss peak (ZLP) width of down to 0.36 eV, with a point spread function drop-off at ~ 2 eV,[62] thus aiding separation of the ZLP from the signal. Typical plasmon lifetimes meant plasmon line widths were very much greater than the energy resolution. Nevertheless, the excellent energy resolution resulted in fine structure of the EEL spectra, the presence of which later proved advantageous for decomposition of spectra into component Gaussian peaks. Objective (collector) aperture semiangles of 5.9 (3.4) mrad were used. All spectra had the ZLP extracted in the region 1.8–3.3 eV, using a power law function. Tests showed this energy window was optimum for not removing structure, or inadvertently introducing artifacts. Growth details of the MWCNTs are presented elsewhere.[63]

B. Extracting the volume mode for varying *b*

Experimental MWCNT EEL spectra are detailed in Fig. 10. In these spectra, the π-volume mode was modeled as a single Gaussian peak, G_v, fitted by minimizing the χ^2 value. The resonance energy and line width of the Gaussian peak, appropriate for the impact parameter, were obtained from Fig. 9. The experimental spectra were fitted with one further Gaussian peak, in order to model π-surface contributions. Dynamical polarizability simulations, detailed in the following section, demonstrated dimensions of the thin and thick MWCNTs represented the strong and weak π-surface mode coupling regimes, respectively. π-surface contributions in the strong coupling regime, consisting of multipolar modes or order ℓ, can be approximated as a single peak.[64] For the thick MWCNT, the intensity of G_v was normalized for $b=0$, with the intensity of G_v scaled for larger b; the scaling factor was easily deduced from the simulated π-volume mode intensities detailed in Fig. 9. The intensity scaling procedure was not performed for G_v of the thin MWCNT spectra, owing to the *Begrenzungseffect*.[65,66] Therefore, for the thin MWCNT, the π-volume mode intensity was estimated by minimizing the χ^2 value, in the fitting of G_v to the spectra. Since volume contributions in the thin MWCNT spectra were relatively small in intensity, compared to those of surface contributions, and since the resonance energy and line width of G_v were known quantities, this proved to be straightforward.

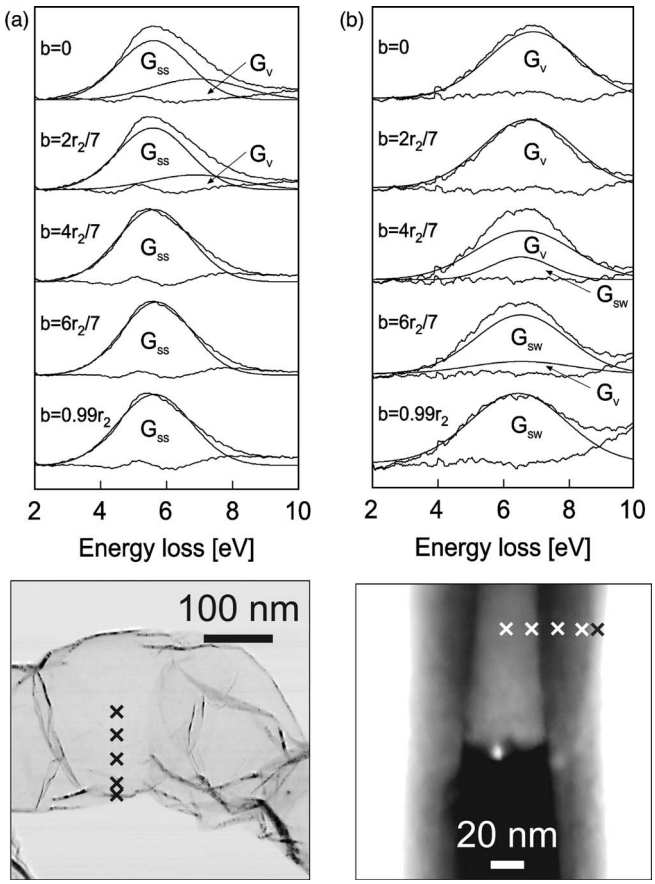

FIG. 10. Experimental EEL spectra decomposed into component Gaussian peaks. Spectra acquired from (a) a thin MWCNT of $r_1=117$ nm, $r_2=121$ nm, $r_1/r_2=0.97$, and (b) a thick MWCNT of $r_1=15$ nm, $r_2=51$ nm, $r_1/r_2=0.29$. In some instances, the energy resolution is sufficiently good to enable maxima of resonances in the fine structure to be actually distinguished. It is noted these maxima correspond well to the maxima of the component Gaussian peaks. Associated BF images are also shown, demonstrating the MWCNT dimensions are sufficient to allow both MWCNTs to be locally approximated as planar media. Key: $G_v=\pi$-volume mode, $G_{ss}=\pi$-surface contributions in the strong coupling regime, $G_{sw}=\pi$-surface contributions in the weak coupling regime.

Immediately evident is the excellent fit of G_v to the thick MWCNT spectrum at $b=0$, which is not unexpected, since the spectrum should consist almost entirely of volume mode contributions. The good fit thus attests to the accuracy of the volume mode model. A measured EEL spectrum results from the convolution of the response of the MCWNT with the finite size of the probe.[54] A change in MWCNT size modifies the relative weight of the volume and surface contributions for a given b.[54] This is evident by comparing spectra at $b=0$ for both the thin and thick MWCNTs. $I_{s,v}$ can be defined as the intensity ratio between the π-surface Gaussian peak to the π-volume Gaussian peak. For each MWCNT, from $b=0$ to $b=0.99r_2$, $I_{s,v}$ is seen to increase.

This can be ascribed to the dual effect of the decrease in volume mode intensity, as detailed in Fig. 9, and the increase in cross section of surface contributions. These two combined effects result in an apparent decrease in energy with b for each MWCNT, of the "composite" π-peak which has not been decomposed into bulk and surface contributions. This decrease in energy has in the past been incorrectly assigned as "redshift" of the composite π-peak.[56] The resonance energy of the modeled volume and surface contributions in Fig. 10 lead one to strongly suspect the 6.4 eV and 5.2 eV peaks measured by Kuzuo *et al.*[67] in EEL spectra of MWCNTs are, in fact, volume and surface plasmons, respectively.

Literature[30] details the energy and intensity shift of measured collective modes of carbon nanospheres with b, being more gradual than those of simulations. This phenomenon is observed for a range of nanosphere dimensions, and can be ascribed to scattered electrons not being collected from an infinitely small area,[30] resulting in "smearing" of abrupt changes in parameter. This may result in minor discrepancies between the modeled and measured π-volume mode. Beam broadening effects may additionally result in wider experimental resonances than those of simulations.[30] Reference 32 compares simulations of multiwall carbon nanosphere EEL spectra, modeled utilizing both EEL data and optical data for the graphite dielectric tensor. The simulation comprised of an anisotropic classical dielectric response approach. A negligible difference for the π-structure between the two models was observed for all b. Therefore, the use of optical data for modeling the EEL response of MWCNTs does not seem likely to have introduced any discrepancies between the modeled and measured volume mode.

A redshift of surface contributions excited on highly oriented pyrolytic graphite, with decreasing in-plane momentum transfer, has previously been observed.[7] This was ascribed to the influence of a band of interband transitions correcting the surface plasmon eigenenergy. With decreasing in-plane momentum transfer, the band of interband transitions shifts in energy away from the surface plasmon eigenenergy, leading to a reduction in influence.[7] In the present case, $\Delta\mathbf{q}_{\perp c}(\alpha_0,\theta,\psi)$ is equivalent to the in-plane momentum transfer. Since $\Delta\mathbf{q}_{\perp c}(\alpha_0,\theta,\psi)$ decreases with b (as seen from the decreasing weighting of $\varepsilon_{\perp c}$ with b, as discussed in Sec. V), for each MWCNT, the decreasing eigenenergy of the π-surface Gaussian peak with increasing b is not surprising.[55] This redshifting would be reduced only weakly by a blueshifting of surface contributions, arising from the increasing weighting of higher order ℓ modes with increasing b.[55,68,69] Furthermore, the relatively large $r_{1,2}$ parameters of the present MWCNTs would suppress curvature effects, e.g., a reduced number of electrons participating in the plasmon oscillation or a higher effective electron mass,[30] either of which could result in modification of measured resonance energies.

The semimetallic band structure of graphite allows vertical interband transitions even at small wave vectors.[7] The weakly coupled surface mode lifetime is dictated by the decay of the surface plasmon into these excitations, which is now discussed. Lin and Shung[70] ascribe the profile of the dielectric response to the number of available channels of optically induced interband transitions. The in-plane component of the volume mode wave vector $\Delta\mathbf{q}_{\perp c}(\alpha_0,\theta,\psi)$, also represents the wave vector of surface contributions. The parameter $\Delta\mathbf{q}_{\perp c}(\alpha_0,\theta,\psi)$ dictates the width of the surface mode in the weak coupling regime; this is easiest to visualize with the π-band shifted by $\Delta\mathbf{q}_{\perp c}(\alpha_0,\theta,\psi)$.[4] Since $\Delta\mathbf{q}_{\perp c}(\alpha_0,\theta,\psi)$ decreases with b, the number of surface mode decay channels increases. Therefore, the weakly coupled surface mode lifetime decreases, and the associated line width consequently increases.[7] This accounts for the line width of the weakly coupled graphite surface mode increasing with b. The increase in weighting of higher order ℓ modes with increasing b would also result in an apparent increase in width of the weakly coupled graphite surface mode with b. One cannot form a simple relationship between $\Delta\mathbf{q}_{\perp c}(\alpha_0,\theta,\psi)$ and the line width of surface contributions in the strong coupling regime, owing to these line widths being governed by a number of factors.[71] One would expect a smaller width of the weakly coupled MWBNNT compared to MWCNT surface modes, ascribed to fewer decay channels arising from the steeper bands of the BN band structure.

C. The weak and strong coupling regimes

A primary electron penetrating a MWCNT loses energy through resonant interaction with the nanotube. In addition to the volume mode, this interaction also excites surface modes on the inner and outer MWCNT walls. As the number of walls of the MWCNT decreases, the degree of interaction between the surface waves on the inner and outer walls increases, resulting in mutually coupled surface modes.[64,72] Numerous literature exists[71] detailing the coupled surface-mode eigenfrequencies of metal foils, which can be modified owing to the depolarizing effect of dielectric coatings. Similarly, the number of walls of a MWCNT dictates the coupled surface-mode eigenfrequency, which can be corrected according to the presence of a dielectric filling and/or dielectric surround of the MWCNT.

In order to demonstrate this phenomenon, a dynamical polarizability model was utilized,[64] providing simulated absorption spectra of coupled π-surface modes excited by aloof primary electrons, on a MWCNT approximated as a spherical anisotropic multiwalled carbon nanosphere. Whilst the spherical approximation simplified calculations, the anisotropy of the MWCNT was preserved. Dynamical screening dictates the energy transfer between the primary beam and surface modes excited on the MWCNT. The simulation allowed the MWCNT to be modeled as possessing a dielectric filling and/or dielectric surround, of high-frequency dielectric constant ε_i and ε_e, respectively. A value of 4.9 was used for the high-frequency dielectric constant of AgI,[73] AgI was the filling of MWCNTs later scrutinized in this contribution. Using the dynamical polarizability model, literature[64] describes interpolation of the $\ell=1$ π-absorption spectrum peak, for the entire parameter range of $r_1/r_2=0$ to $r_1/r_2=1$. Using a similar interpolation method, a single Gaussian peak was fitted to the simulated π-absorption spectra, for various combinations of ε_i, ε_e. The results are summarized in Fig. 11 for the $\ell=1$ mode, higher order modes exhibit similar trends for the ε_i, ε_e combinations.

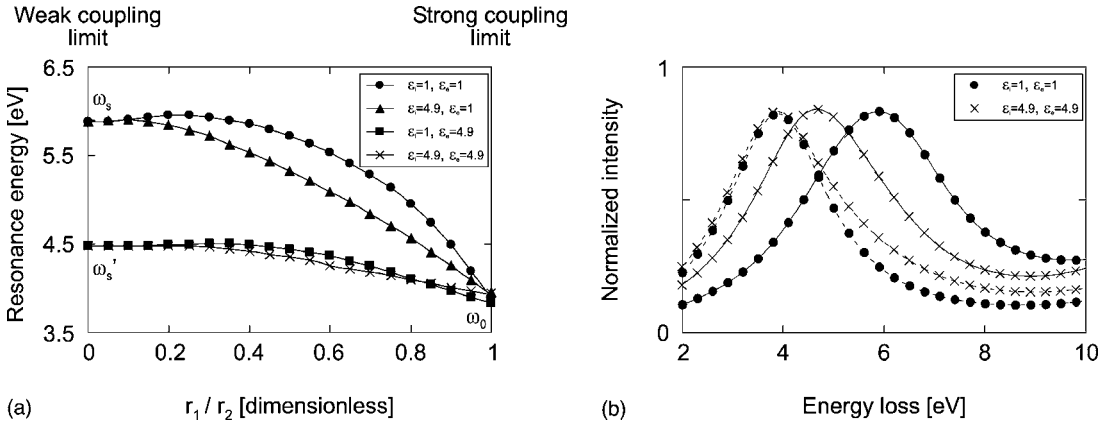

FIG. 11. (a) $\ell=1$ mode π-absorption spectra eigenfrequency curves for the MWCNT, modeled as a multiwalled carbon nanosphere, for various combinations of a dielectric filling and a dielectric surround, of constants ε_i, ε_e, respectively. Note for all ℓ modes, ω_0, ω_s and ω_s' remain invariant. (b) $\ell=1$ mode simulated loss spectra at the strong (dashed line) and weak (solid line) coupling limits for an unfilled and unsurrounded MWCNT, and a filled and surrounded MWCNT, both modeled as a multiwalled carbon nanosphere.

The simulated spectra consist of contributions related to (lower energy) symmetrical and (higher energy) asymmetrical π-surface field configurations. The symmetrical and asymmetrical field configurations can be associated with $\varepsilon_{\|c}$ and $\varepsilon_{\perp c}$, respectively.[74] Owing to the dipole length associated with the former, always being larger than that of the latter,[55] the Gaussian peak fitted to the simulated π-absorption spectra may be considered as representing the lower energy symmetrical modes, and may further be considered as analogous to the coupled ω_- mode of a thin metal foil.[71] Therefore ω_s and ω_s', representing the Gaussian peak thick limit asymptote energy at $r_1/r_2 \to 0$ for the various combinations of ε_i, ε_e, can be qualitatively compared to the ω_- coupled surface mode thick limit asymptote energy of a planar metal foil, bounded on one or both sides by a semi-infinite dielectric medium of $\varepsilon > 1$. The higher energy asymmetrical modes of a MWCNT (not shown in Fig. 11) approach a thick limit asymptote as $r_1/r_2 \to 0$, i.e., the same trend observed for the ω_+ mode as a thin metal foil increases in thickness.[70]

Considering the dipole mode, Fig. 11 demonstrates the thick limit asymptote energy is identical for both the MWCNT with $\varepsilon_i=1$, $\varepsilon_e=1$, and the MWCNT with $\varepsilon_i=4.9$, $\varepsilon_e=1$. For the latter, one would expect ω_s to be redshifted, i.e., behavior observed for the ω_- mode of a metal foil coated only on one side with a semi-infinite dielectric.[71] The observed behavior for the MWCNT with $\varepsilon_i=4.9$, $\varepsilon_e=1$, with ω_s remaining unmodified in resonance energy, represents similar behavior as observed for the ω_- mode of a metal foil embedded in vacuum.[71] Therefore, the *filled* and *unsurrounded* MWCNT appears to respond as though it were *unfilled* and *unsurrounded*.

One can imagine this occurs due to the dynamical polarizability model describing a plasmon excitation by a locally nonchanging (i.e., uniform) field, with only one ℓ mode excited. Dominance of the $\ell=1$ mode occurs when a localized source is far away from an excitation. For an outside probe, the scenario may be intuitively interpreted as due to polarization effects at the outer surface, so that screening occurs and the filling becomes ineffective. (The inside does not "see" the excitation on the outside.) Curiously, for the MWCNT with $\varepsilon_i=4.9$, $\varepsilon_e=1$, between the thick and thin limits, Fig. 11 shows a difference in the eigenenergy of maximal $\sim$0.44 eV, with respect to the case when $\varepsilon_i=1$, $\varepsilon_e=1$. From the screening argument, one should not expect such splitting. In the present experiment, however, the field originates from a localized probe close to, or even penetrating, the nanotube so that the $\ell=1$ assumption is not valid. Calculations including a number of ℓ modes (1 to 10), which represent a nearby probe more appropriately, indicate that the two "vacuum" branches (i.e., those for $\varepsilon_i=1$, $\varepsilon_e=1$ and $\varepsilon_i=4.9$, $\varepsilon_e=1$) do in fact merge (see explanation in the following paragraph).

Analogous observations apply for the filled and surrounded, and the unfilled and surrounded, MWCNTs in Fig. 11. Here, the eigenenergy for all r_1/r_2 parameters is nearly identical for both the MWCNT with $\varepsilon_i=4.9$, $\varepsilon_e=4.9$, and the MWCNT with $\varepsilon_i=1$, $\varepsilon_e=4.9$. The already small difference between these "dielectric" branches vanishes when a number of ℓ modes is included in the calculations. Notably, the redshift of ω_s to ω_s' at the thick limit represents behavior observed for the ω_- mode of a metal foil bounded on one side by a dielectric or bounded on both sides by a dielectric.[71] As intuitively argued before, the polarization of the MWCNT outer surface results in screening of the MWCNT inner wall. Therefore, it is impossible to deduce whether the MWCNT with $\varepsilon_e=4.9$ is filled or unfilled.

Hence, merely the dielectric surround dictates the degree of redshifting of MWCNT coupled surface contributions. This phenomenon is experimentally validated in the following final section.

D. Extracting the volume mode for $b=0$

Figure 12(a) represents a STEM bright field (BF) image of a MWCNT partially filled with a dielectric. The filled region is reminiscent of dielectric and metal nanocylinder composites,[68,75,76] nanowires,[77] and metal-filled MWCNTs.[78]

In EEL spectra of metal nanospheres possessing small r_2, the dipole mode is seen to dominate surface contributions in the aloof geometry.[79] However, as already mentioned, for the

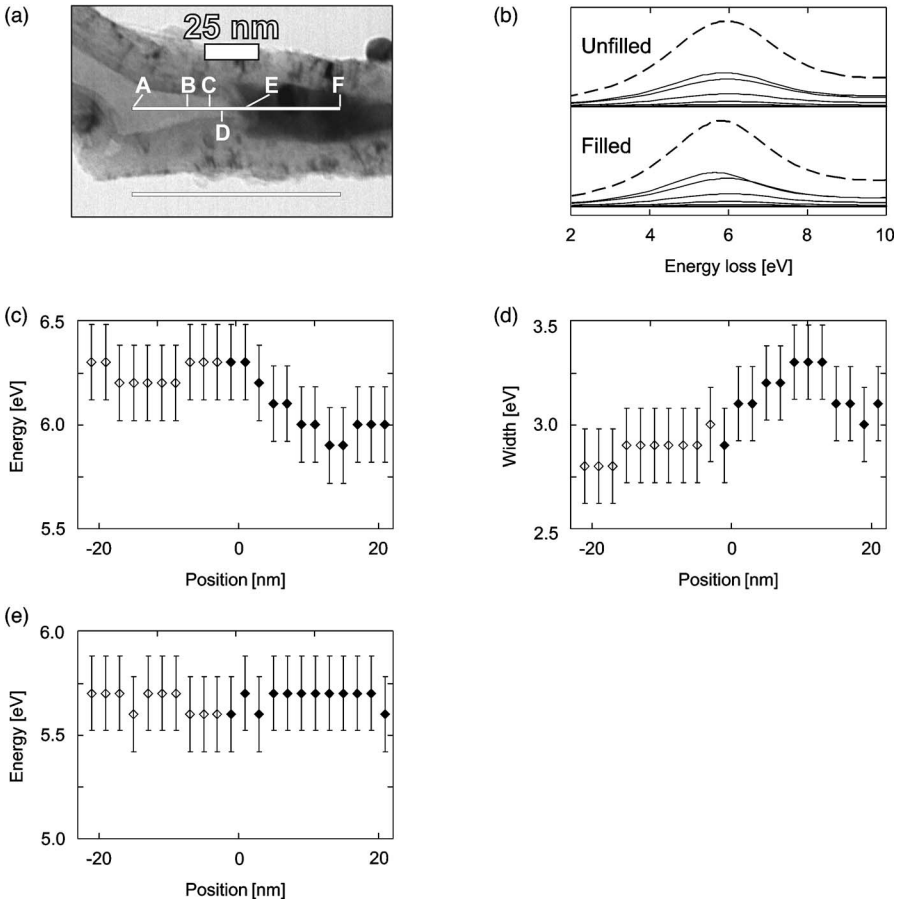

FIG. 12. (a) STEM BF image of a partially filled MWCNT. (b) Dynamical polarizability simulations at aloof positions adjacent to the interface. The dashed lines represent the sum of modes $\ell = 1, \ldots, 10$. At each position, each ℓ mode from 1 to 10 has a progressively lower intensity. (c) Surface Gaussian peak energies, deduced using the volume mode model to extract volume contributions. Spectra were acquired in the penetrating mode, along the line *AF* identified in (a). (d) Width of the composite π peak. (e) Surface Gaussian peak energies, deduced from aloof spectra acquired along the line identified in (a). Uncertainty in measured parameters was estimated at $1/2\times$ energy resolution. Unfilled (filled) markers represent the surface Gaussian peak in the unfilled (filled) region, gray markers represent the peak in the interface region.

MWCNT detailed in Fig. 12(a), the dipole condition[69] $\omega r_2/v \ll 1$ is not met, hence the $\ell=1$ mode cannot be assumed to dominate aloof spectra; this results in coupled π-surface contributions consisting of multipolar modes of order ℓ. Such multipolar modes can be approximated as a single peak,[64] with individual ℓ modes remaining unresolved, even with a spectrometer energy resolution approaching the theoretical limit for a cold field-emission gun.[55]

This lack of resolution of individual ℓ modes is of paramount importance, since the measured parameters of the π-surface contribution in a MWCNT EEL spectrum are then dictated by the superposition of weighted ℓ modes.[55] Dynamical polarizability simulations are detailed in Fig. 12(b), which were calculated using the same equations as those for Fig. 11. Figure 12(b) demonstrates that in both the unfilled and filled regions, the $\ell=2$ mode has a significant intensity compared to that of the $\ell=1$ mode. The $\ell=1$ mode has an energy of 5.90 eV (5.65 eV) in the unfilled (filled) regions. However, the superposition of multipolar ℓ modes results in a "smearing" of the $\ell=1$ mode; the peak of the sum of modes $\ell=1, \ldots, 10$ has an energy of 5.95 eV (5.8 eV) in the unfilled (filled) regions. The splitting into two branches of the "vacuum" dipole mode ($\varepsilon_i=1$, $\varepsilon_e=1$ and $\varepsilon_i=4.9$, $\varepsilon_e=1$; see Fig. 11) for an unfilled and filled MWCNT thus remains obscured.

The MWCNT detailed in Fig. 12(a) possessed several criteria, which were critical for testing energy shifting of surface contributions, due to the presence of a dielectric filling:

(i) the filling was composed of AgI; the resonance energy of silver and iodine plasmon features are sufficiently high to prevent the carbon π-features from being obscured;

(ii) the MWCNT possessed a range of thicknesses, enabling one to test for effects of the changing aspect ratio r_1/r_2;

(iii) there is an interface between an unfilled and filled region, enabling one to test for a redshift of surface contributions in the dielectric;

(iv) since $\omega r_2/v \sim 1.8$ and $v/c < 1$, relativistic effects were considered to be small, with a nonretarded approximation reasonable;[80,81] and

(v) the range of values of r_1, r_2 meant quantum size effects[28–30] could also be neglected.

Spectra were acquired along the lines indicated in Fig. 12(a). For spectra acquired in the penetrating geometry, the π-volume mode was modeled as a single Gaussian peak, fitted by minimizing the χ^2 value. The resonance energy and line width of the Gaussian peak, appropriate for $b=0$, were obtained from Fig. 9. For $b=0$, these parameters are seen to be invariant with $r_{1,2}$; the nonuniform $r_{1,2}$ parameters of the present MWCNT were therefore of no consequence. One further Gaussian peak was fitted to these spectra, in order to model π-surface contributions. For spectra acquired in the aloof mode, modeling the π-volume mode was unnecessary, owing to the volume mode cross section vanishing in the nonpenetrating geometry. Solely one Gaussian peak was therefore fitted to aloof spectra, thus modeling π-surface contributions.

To conclude the discussion in the previous section regarding Fig. 11, we stated that as a result of dynamical screening,

when a localized probe passes a MWCNT wall on one side, the other side does not "know" of this (hence no response). The MWCNT in Fig. 12(a) is so large, that when the probe proceeds in the penetrating geometry through the center ($b=0$), it spends most of the transit time in vacuum or in the dielectric filling inside the MWCNT, residing for only a negligible amount of time in the MWCNT wall (top and bottom). The $b=0$ situation can therefore be seen as an "aloof probe on the inside" and can hence be described by the "dielectric" branch in Fig. 11, i.e., by the scenario of a probe passing through a dielectric surround in the vicinity of a nanotube. The surface contribution energy, when exciting through the dielectric, is redshifted by ~0.5 eV. This compares to a predicted energy "gap" of ~1 eV between the upper (vacuum) branches and the lower (dielectric) branch in Fig. 11, at the respective r_1/r_2 ratio of around 0.4 (e.g., at the interface with the dielectric). The r_1/r_2 values in Fig. 12(a) range from 0.2 to 0.4, with most values in the interval 0.38–0.4. Hence, the theoretical and experimental redshift values differ by an amount not covered by the error bars. However, considering the simplicity of the model (only including the $\ell=1$ mode) and the inaccuracies in determining wall thicknesses from cylindrical projections in diffraction contrast images, as well as "artificial thickening" of the wall through amorphization at the outside, the agreement between prediction and experiment is not unreasonable.

In order to confirm the measured energy discontinuity in the surface Gaussian peak at the interface is not artificial, the changing linewidth of a *single* Gaussian peak fitted to the *composite* π-peak (i.e., consisting of both π-volume and π-surface contributions) is provided in Fig. 12(d). This method eliminated any uncertainties introduced from the modeling of the π-volume mode. The increase in linewidth of the composite peak by ~0.4 eV from the unfilled to the filled region, is concomitant with redshifted surface contributions of precisely the same magnitude.

Figure 12(e) details the measured energy of a single Gaussian peak fitted to the aloof spectra. The energy is practically invariant at ~5.6 eV. The presence of the dielectric filling discontinuity therefore appears to have *no effect* on the measured energy of surface features excited in the (outside) aloof mode. The reason for the lack of surface mode eigenenergy shifting in these measurements can be understood from issues discussed in the previous paragraph, regarding Fig. 11. Since in the outside-aloof mode the probe proceeds through the same medium, i.e., vacuum, at all locations, the energies are represented by the "vacuum" branch in Fig. 11, i.e., there will be no shift in the energy of the outer wall resonance expected from a change of the internal dielectric constant. There will be no change of the outer wall resonance expected from a change in wall thickness either: the r_1/r_2 ratio has a maximum change from 0.2 to 0.4, with most values between 0.38 and 0.4. The accompanying energy shift, at most, is expected to be 0.3 eV, in the "vacuum" branch (Fig. 11); for the majority of points it will be <0.1 eV. There is a slight dip in the energy value concomitant with the position of largest change in r_1/r_2 near the interface in Fig. 12(e). However, for all positions the predicted shift would lie within the experimental error, this means there is good agreement between experimental results and theory.

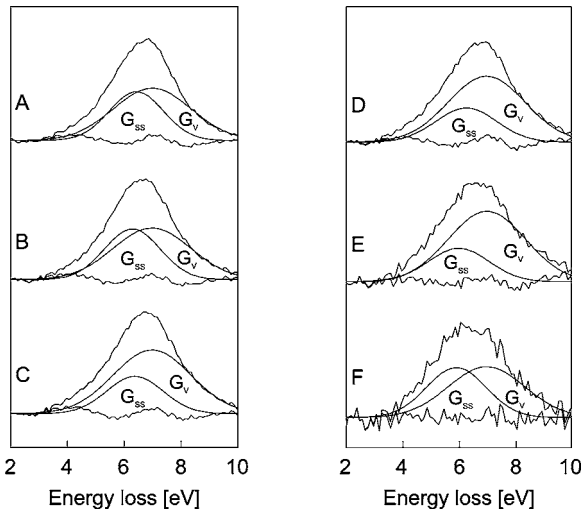

FIG. 13. Decomposed spectra, acquired at locations along *AF* identified in Fig. 12(a). Key: $G_v=\pi$-volume mode, G_{ss}=coupled π-surface mode. Spectra are unsmoothed, in order to demonstrate the decreasing signal-to-noise ratio from the unfilled to the filled region.

Decomposed spectra are illustrated in Fig. 13, for various positions along *AF* identified in Fig. 12(a). Positions *C*, *D*, and *E* represent the thickest part of the MWCNT; hence, the spectra are dominated by volume contributions. The redshift of the surface Gaussian peak from position *D* to *E* is evident, as is the decreasing signal-to-noise ratio from the unfilled to filled regions. At each position, the good fit is demonstrated by the low residual.

Interface plasmons arise from the *Begrenzungseffect*[65,66] and are excited when a primary beam propagates parallel to the vicinity of an interface between two media.[82] The interface plasmon is localized to the interface, with the intensity decaying exponentially with perpendicular distance from the interface; an interface plasmon typically becomes vanishing in intensity at a distance of $\sim>15$ nm from the interface.[82] The surface Gaussian peak energy of 5.9 eV at position *F*, lying ~40 nm from the interface, provides explicit proof that the measured energy gap observed in Fig. 12(c) does not arise from excitation of an interface plasmon. Spectra acquired at other positions, far from the interface, confirm this interpretation.

In summary, the dynamical polarizability model of Fig. 11 details redshifting of coupled surface features occurs through two mechanisms: firstly from the presence of a dielectric filling, and secondly from the decrease in local thickness of the MWCNT. The effect of a filling does not show up in aloof measurements; in order to see it, the localized probe has to penetrate the filling. The results thus demonstrate the value of the present volume mode model, in resolving obscured features in MWCNT EEL spectra acquired in the penetrating geometry.

VII. SUMMARY

The direction of the plasmon wave vector with respect to the crystal planes dictates the matrix element of collective

excitations in anisotropic media. Variations in the matrix element as a function of crystal orientation have been studied by highly spatially resolved EELS. Corrections accounting for the lowering of symmetry ascribed to optical anisotropy and cylindrical anisotropy, by deducing the intrinsic scattering kinematics of primary electrons in **k** space, have been utilized to model the volume mode EEL function for a graphite and a BN slab. The model is generic in nature and can be applied to any anisotropic lamellar material, e.g., graphite intercalation compounds (GICs).

Simulations of the dynamical polarizability of a MWCNT by STEM primary electrons result in the remarkable prediction of whether of not a MWCNT possessing dimensions consistent with the *decoupled* regime is filled with a dielectric that allows the surface mode eigenfrequency to be modified. In order to experimentally verify this phenomenon, it was essential to utilize the simulated π-volume mode model, in order to extract π-volume mode contributions from EEL spectra acquired in the penetrating geometry. The eigenfrequency modification remains hidden in EEL spectra acquired in the aloof geometry. The present findings thus directly challenge the long-held belief of the microscopy community of the aloof geometry being superior to penetrating geometry for examining surface modes.

*Corresponding author.

[1] P. E. Batson, Ultramicroscopy **47**, 133 (1992).
[2] C. Colliex, Ultramicroscopy **18**, 131 (1985).
[3] R. D. Leapman, P. L. Fejes, and J. Silcox, Phys. Rev. B **28**, 2361 (1983).
[4] K. Zeppenfeld, Opt. Commun. **1**, 119 (1969).
[5] W. Baronian, Mater. Res. Bull. **7**, 119 (1972).
[6] J. F. Annett, R. E. Palmer, and R. F. Willis, Phys. Rev. B **37**, 2408 (1988).
[7] P. Laitenberger and R. E. Palmer, Phys. Rev. Lett. **76**, 1952 (1996).
[8] D. M. Hoffman, G. L. Doll, and P. C. Eklund, Phys. Rev. B **30**, 6051 (1984).
[9] C. Tarrio and S. E. Schnatterly, Phys. Rev. B **40**, 7852 (1989).
[10] R. A. Rosenberg, P. J. Love, and V. Rehn, Phys. Rev. B **33**, 4034 (1986).
[11] N. D. Browning, J. Yuan, and L. M. Brown, Ultramicroscopy **38**, 291 (1991).
[12] N. D. Browning, J. Yuan, and L. M. Brown, Philos. Mag. A **67** (1), 261 (1993).
[13] K. Zeppenfeld, Z. Phys. **243B**, 229 (1971).
[14] K. Zeppenfeld, Z. Phys. **25A**, 335 (1967).
[15] Y. H. Ichikawa, Phys. Rev. **109**, 653 (1958).
[16] A. G. Marinopoulos, L. Reining, V. Olevano, and A. Rubio, Phys. Rev. Lett. **89**, 076402 (2002).
[17] L. S. Caputi, G. Chiarello, A. Santaniello, E. Colavita, and L. Papagno, Phys. Rev. B **34**, 6080 (1986).
[18] R. E. Palmer, J. F. Annett, and R. F. Willis, Phys. Rev. Lett. **58**, 2490 (1987).
[19] W.-H. Soe, A. M. Shikin, F. Moresco, V. K. Adamchuk, and K.-H. Rieder, Phys. Rev. B **64**, 235404 (2001).
[20] S. Iocobucci, P. Letardi, M. Montagnoli, P. Nataletti, and G. Stefani, J. Electron Spectrosc. Relat. Phenom. **67**, 479 (1994).
[21] U. Büchner, Phys. Status Solidi B **81**, 227 (1977).
[22] R. Klucker, M. Skibowski, and W. Steinmann, Phys. Status Solidi B **65**, 703 (1974).
[23] K. Zeppenfeld, Z. Phys. **211**, 391 (1968).
[24] G. L. Doll, *Handbook of Optical Constants of Solids*, edited by E. D. Palik, Vol. 3 (Academic, New York, 1998), p. 425.
[25] D. L. Greenaway, G. Harbeke, F. Bassani, and E. Tosatti, Phys. Rev. **178**, 1340 (1969).
[26] L. Laffont, M. Monthioux, and V. Serin, Carbon **40**, 767 (2002).
[27] H. Ibach and D. L. Mills, *Electron Energy Loss Spectroscopy and Surface Vibrations* (Academic, New York, 1982), p. 74.
[28] C. Yannouleas, E. N. Bogachek, and U. Landman, Phys. Rev. B **50**, 7977 (1994).
[29] C. Yannouleas, E. N. Bogachek, and U. Landman, Phys. Rev. B **53**, 10225 (1996).
[30] T. Stöckli, J.-M. Bonard, A. Châtelain, Z. L. Wang, and P. Stadelmann, Phys. Rev. B **61**, 5751 (2000).
[31] E. Evans and D. L. Mills, Phys. Rev. B **5**, 4126 (1972).
[32] T. Stöckli, J.-M. Bonard, A. Châtelain, Z. L. Wang, and P. Stadelmann, Phys. Rev. B **57**, 15599 (1998).
[33] B. Jouffrey, P. Schattschneider, and C. Hébert, Ultramicroscopy **102**, 61 (2004).
[34] C. Souche, B. Jouffrey, G. Hug, and M. Nelhiebel, Micron **29**, 419 (1998).
[35] D. Pines, Rev. Mod. Phys. **28**, 184 (1956).
[36] R. F. Egerton, *Electron Energy-Loss Spectroscopy in the Electron Microscope*, 2nd ed. (Plenum, New York, 1996), p. 162.
[37] T. Stöckli, J.-M. Bonard, A. Châtelain, Z. L. Wang, and P. Stadelmann, Appl. Phys. Lett. **80**, 2982 (2002).
[38] A. Borghesi and G. Guizzetti, *Handbook of Optical Constants of Solids*, edited by E. D. Palik, Vol. 2 (Academic, New York, 1998), p. 449.
[39] L. Henrard, O. Stéphan, M. Kociak, C. Colliex, and Ph. Lambin, J. Electron Spectrosc. Relat. Phenom. **114-116**, 219 (2001).
[40] J. Daniels, C. v Festenberg, H. Raether, and K. Zeppenfeld, Springer Tracts Mod. Phys. **54**, 123 (1970).
[41] O. Stéphan, M. Kociak, L. Henrard, K. Suenaga, A. Gloter, M. Tencé, E. Sandré, and C. Colliex, J. Electron Spectrosc. Relat. Phenom. **114**, 209 (2001).
[42] A. J. Gatesman, R. H. Giles, and J. Waldman, J. Appl. Phys. **73**, 3962 (1993).
[43] H. Raether, Springer Tracts Mod. Phys. **88**, 18 (1980).
[44] B. T. Draine, Astrophys. J., Suppl. Ser. **57**, 587 (1985).
[45] B. T. Draine and H. M. Lee, Astrophys. J. **285**, 89 (1984).
[46] T. Stöckli, J.-M. Bonard, A. Châtelain, Z. L. Wang, and P. Stadelmann, Phys. Rev. B **64**, 115424 (2001).
[47] H. G. Wessjohann, Z. Phys. **269**, 269 (1974).
[48] E. Tossati, Nuovo Cimento B **63**, 54 (1969).
[49] T. Stöckli, Z. L. Wang, J.-M. Bonard, P. Stadelmann, and A. Châtelain, Philos. Mag. B **79**, 1531 (1999).
[50] T. Pichler, M. Knupfer, M. S. Golden, J. Fink, A. Rinzler, and R. E. Smalley, Phys. Rev. Lett. **80**, 4729 (1998).
[51] A. G. Marinopoulos, L. Reining, A. Rubio, and N. Vast, Phys.

Rev. Lett. **91**, 046402 (2003).
[52] B. W. Reed and M. Sarikaya, Phys. Rev. B **64**, 195404 (2001).
[53] F. L. Shyu and M. F. Lin, Phys. Rev. B **62**, 8508 (2000).
[54] M. Kociak, L. Henrard, O. Stéphan, K. Suenaga, and C. Colliex, Phys. Rev. B **61**, 13936 (2001).
[55] A. Seepujak, U. Bangert, A. Gutiérrez-Sosa, A. J. Harvey, V. D. Blank, B. A. Kulnitskiy, and D. V. Batov, Ultramicroscopy **104**, 57 (2005).
[56] L. A. Bursill, P. A. Stadelmann, J. L. Peng, and S. Prawer, Phys. Rev. B **49**, 2882 (1994).
[57] M. F. Lin, C. S. Huang, and D. S. Chuu, Phys. Rev. B **55**, 13961 (1997).
[58] J. A. Hunt, F. E. Dickerson, A. A. Abbott, G. Szantai, and P. E. Mooney, *UHV Enfina—A New High-Performance EELS Spectrometer for the VG STEM. Microscopy and Microanalysis 2001 Proceedings*, Vol. 7, Suppl. 3, p. 1132.
[59] M. Tencé, M. Quartuccio, and C. Colliex, Ultramicroscopy **58**, 42 (1995).
[60] C. Jeanguillaume and C. Colliex, Ultramicroscopy **28**, 252 (1989).
[61] J. A. Hunt and D. B. Williams, Ultramicroscopy **38**, 47 (1991).
[62] A. Gutiérrez-Sosa, U. Bangert, A. J. Harvey, C. J. Fall, R. Jones, P. R. Briddon, and M. I. Heggie, Phys. Rev. B **66**, 035302 (2002).
[63] P. M. F. J. Costa, J. Sloan, J. L. Hutchison, and M. L. H. Green, Chem. Commun. (Cambridge) **18**, 2276 (2003).
[64] A. A. Lucas, L. Henrard, and Ph. Lambin, Phys. Rev. B **49**, 2888 (1994).
[65] F. J. García de Abajo and P. M. Echenique, Phys. Rev. B **45**, 8771 (1992).
[66] P. M. Echenique, J. Bausells, and A. Rivacoba, Phys. Rev. B **35**, 1521 (1987).
[67] R. Kuzuo, M. Terauchi, and M. Tanaka, Jpn. J. Appl. Phys., Part 2 **31**, L1484 (1992).
[68] C. A. Walsh, Philos. Mag. A **59**, 227 (1989).
[69] P. M. Echenique, A. Howie, and D. J. Wheatley, Philos. Mag. B **56**, 335 (1987).
[70] M. F. Lin and Kenneth W.-K. Shung, Phys. Rev. B **50**, 17744 (1994).
[71] H. Raether, Springer Tracts Mod. Phys. **38**, 84 (1965).
[72] M. Šunjić and A. A. Lucas, Phys. Rev. B **3**, 719 (1971).
[73] I. L. Mladenovic, W. K. Kegel, P. Bomans, and P. M. Frederik, J. Phys. Chem. B **107**, 5717 (2003).
[74] M. Kociak, O. Stéphan, L. Henrard, V. Charbois, A. Rothschild, R. Tenne, and C. Colliex, Phys. Rev. Lett. **87**, 075501 (2001).
[75] J. M. Pitarke, F. J. García-Vidal, and J. B. Pendry, Phys. Rev. B **57**, 15261 (1998).
[76] U. Schröter and A. Dereux, Phys. Rev. B **64**, 125420 (2001).
[77] G. F. Bertsch, H. Esbensen, and B. W. Reed, Phys. Rev. B **58**, 14031 (1998).
[78] F. J. García-Vidal, J. M. Pitarke, and J. B. Pendry, Phys. Rev. B **58**, 6783 (1998).
[79] T. L. Ferrell and P. M. Echenique, Phys. Rev. Lett. **55**, 1526 (1985).
[80] F. J. García de Abajo and A. Howie, Phys. Rev. Lett. **80**, 5180 (1998).
[81] F. J. García de Abajo, Phys. Rev. B **59**, 3095 (1999).
[82] P. Moreau, N. Brun, C. A. Walsh, C. Colliex, and A. Howie, Phys. Rev. B **56**, 6774 (1997).